

# Data-Efficient Electromagnetic Surrogate Solver Through Dissipative Relaxation Transfer Learning

Sunghyun Nam<sup>1</sup>, Chan Y. Park<sup>2\*</sup>, and Min Seok Jang<sup>1\*</sup>

<sup>1</sup>School of Electrical Engineering, Korea Advanced Institute of Science and Technology, Daejeon 34141, Republic of Korea

<sup>2</sup>KC Machine Learning Lab, Seoul 06181, Republic of Korea

\*Corresponding authors: [chan.y.park@kc-ml2.com](mailto:chan.y.park@kc-ml2.com), [jang.minseok@kaist.ac.kr](mailto:jang.minseok@kaist.ac.kr)

## Abstract

In neural-network surrogate solvers for electromagnetic simulations, accurately modeling resonant phenomena remains a central challenge. High-amplitude resonances generate strongly localized field patterns that appear as outlier samples, deviating significantly from the general distribution of non-resonant cases, leading to instability and degraded predictive performance. To address this, we introduce dissipative relaxation transfer learning (DIRTL), a data-efficient training framework that integrates transfer learning with loss-regularized optimization principles from high-Q photonics. DIRTl first pretrains the model on data generated with a small fictitious material loss, which broadens sharp resonant modes and suppresses extreme field amplitudes. This smoothing of the response landscape enables the model to learn global modal features more effectively. The pretrained model is subsequently fine-tuned on the target lossless dataset containing the true high-amplitude resonances, allowing stable adaptation based on the pretrained information. Applied to both the Fourier Neural Operator (FNO) and UNet architectures, DIRTl yields substantial improvements in prediction accuracy, including up to a two-fold error reduction for the FNO variant. Furthermore, DIRTl exhibits robustness across diverse training conditions and supports strong multi-task performance, underscoring the generalizability and flexibility of the pretrained core. Altogether, these results establish DIRTl as a physically grounded and architecture-agnostic curriculum for enhancing the reliability of machine-learning-based electromagnetic solvers.

## 1. Introduction

In recent years, machine learning-based approaches for solving parametric differential equations (PDEs) have gained significant attention, offering promising alternatives to traditional numerical solvers. These methods have been widely explored across various scientific and engineering domains due to their potential advantages, such as computational efficiency, reduced memory requirements, and the ability to approximate complex, nonlinear relationships [1]. In particular, machine learning-driven surrogate solvers have shown great promise in electromagnetic (EM) simulations and nanophotonic design. Conventional numerical techniques for EM simulations, such as the finite-difference time-domain (FDTD) method and rigorous coupled-wave analysis (RCWA), provide accurate solutions but are often computationally expensive, and these act as the bottleneck in iterative inverse design processes. To address these limitations, neural network models have been explored as surrogate solvers to accelerate simulations and facilitate rapid design-space exploration [2,3].

In training neural network-based surrogate solvers for EM simulations, a significant challenge arises when dealing with resonant structures. These systems exhibit strongly localized field confinement, leading to substantial difficulties for standard neural network architectures to capture their field patterns accurately [4-6]. This issue is compounded by the fact that highly resonant cases are scarce in the dataset, and their field patterns deviate from the general scheme of background-only scatterings [7,8]. Consequently, resonant cases act as outliers, causing both underfitting—where resonant cases are not properly captured—and overfitting—where non-resonant cases are predicted as resonances. Most research in PDE solving via neural networks has focused on suppressing these outlier cases [9,10]. However, this approach is not appropriate for EM problems, as resonant modes are crucial in the design of photonic devices [11,12].

Most existing approaches for improving neural network surrogate solvers primarily emphasize model design—modifying network architectures to enhance generalization and expressivity, thereby enabling them to handle more diverse and complex physical systems. For accurate field predictions, neural network models such as DeepONet [13, 14], UNet [8, 15-21], and the Fourier Neural Operator (FNO)[5,6,22-24] have been extensively explored. While these strategies have demonstrated notable performance gains, they remain largely problem-specific, with solutions often tailored to specific datasets or device configurations. More critically, although such methods can alleviate

certain challenges in photonics modeling, they do not directly address the fundamental limitation of EM surrogate models—the intrinsic difficulty of accurately capturing resonant behaviors that dominate many photonic systems.

Another important line of research incorporates physics-based loss functions during learning. In EM systems, this often takes the form of a Maxwell loss, which quantifies how well the surrogate solver adheres to Maxwell's equations. By embedding this physical knowledge directly into the training objective, the model is encouraged to learn physical behavior rather than merely interpolating data—thereby improving data-efficiency and generalization [5, 16-19]. However, a key challenge remains in that, beyond the extreme physics of highly resonant phenomena, the supervised-learning paradigm itself makes it inherently difficult to predict the rare cases of outlying amplitudes.

In this work, we propose a data-driven training framework that combines conventional photonic optimization principles with transfer learning to challenge the obstacles from high-resonant training regimes. Inspired by optimization strategies for high-Q photonic structures—where artificial material loss is introduced to broaden sharp resonances and subsequently removed to recover optimal performance [25-28]—we formulate an analogous two-stage learning process termed *dissipative relaxation transfer learning* (DIRTL). This approach enables smooth convergence and enhanced generalization by guiding the network through a refined learning landscape. As a result, DIRTl achieves substantially improved prediction accuracy with approximately 9-fold sample efficiency, demonstrating its potential as an efficient framework for EM surrogate-solver training. Furthermore, this framework offers an alternative means of implicitly embedding physical knowledge into the learning process, highlighting its potential applicability to a broader range of scientific machine learning problems.

## 2. Dissipative Relaxation Transfer Learning

### 2.1 Problem Description

As a physical problem, we consider a one-dimensional (1D) multi-wavelength binary grating, which is described in Fig. 1(a). The grating consists of a  $1 \times 64$  array in free space, illuminated by a transverse magnetic (TM) plane wave normally incident to the device. Each element alternates between free space and a dielectric material with refractive index  $n = 2$ . The training and testing datasets span wavelengths from 650 nm to 750 nm in 10 nm increments, with all EM field data generated using the `meent` rigorous coupled-wave analysis (RCWA) solver [29]. Simulations employed 81 Fourier orders, which were shown to be sufficient for numerical convergence (see Section 1 of the Supplementary Information).

From this problem setup, we observe the emergence of the resonant outlier cases as described above. As illustrated in Fig. 1(b), most of the generated test samples are non-resonant, not showing pronounced localized field enhancements in the grating space, whilst cases of highly localized fields with large field amplitudes occasionally emerge. This distribution is quantified in Fig. 1(c), displaying a long tail corresponding to strongly resonant cases with maximum amplitudes reaching over 50 times the incident field amplitude.

As the baseline surrogate solver, we employed the Fourier Neural Operator (FNO) model [22] consisting of a lifting layer, a series of Fourier layers, and a projection layer which has been widely adopted in recent electromagnetic simulation studies. Both lifting and projection layers consist of  $1 \times 1$  pointwise convolutions, mapping the input in and out of the iterative Fourier layers. To further examine the general applicability of our training strategy, we also implemented a UNet model, which has demonstrated comparable effectiveness in electromagnetic field prediction and inverse-design tasks [15]. UNet follows the standard encoder-decoder architecture with residual connections, which is commonly used in image segmentation (see Section 4 of the Supplementary Information).

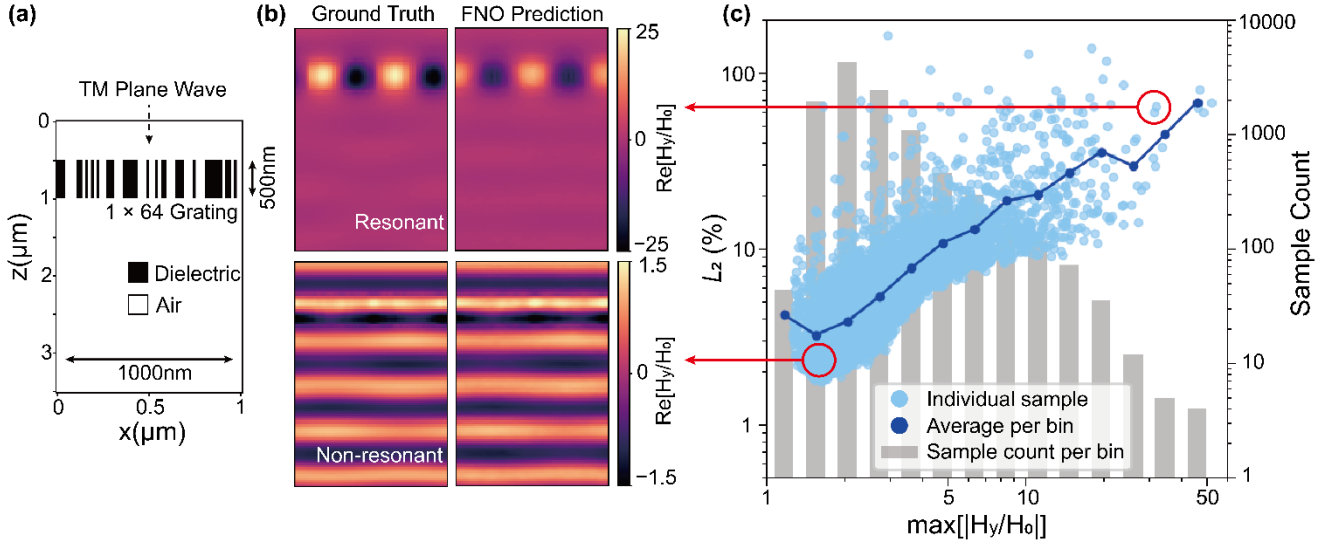


**Figure 1 Problem schematic for DIRTl testing.** (a) Data generation setup. Training samples are produced by randomly generating binary grating structures. (b) Representative field distributions for resonant and non-resonant cases. Resonant structures exhibit strongly localized, high-amplitude fields concentrated within the grating region, whereas non-resonant cases show broadly distributed, weakly varying fields. (c) Baseline FNO performance trained only on lossless target data with the bin-averaged error (blue markers) and the corresponding data-distribution histogram (gray bars). Each light-blue dot indicates the prediction error versus the maximum field amplitude for a single test sample, and blue markers denote the average error within logarithmically spaced amplitude bins. The histogram shows an exponential decrease in sample count with increasing maximum amplitude, with extreme resonant cases (amplitudes approaching 50) comprising less than 0.01% of the dataset. Red circles highlight the locations of the resonant and non-resonant examples from panel (b) within the overall error–amplitude distribution.

To incorporate wavelength information effectively, we adopted the wave prior approach introduced in **NeurOLight** [23]. In this method, the wavelength is encoded as a sinusoidal function that mirrors the incident plane wave, providing both explicit wavelength information and a strong initial guess for the model to refer from. For each training sample, both the device structure and the corresponding wave prior were used as model inputs. The networks were trained using the mean squared error (MSE) loss, whilst optimized by the Adam optimizer [30]. The learning rate was tuned through Bayesian optimization with a step learning rate scheduler, which provided the most stable and efficient convergence. The detailed hyperparameters for both models and learning rates are summarized in Section 4 of the Supplementary Information.

When trained on such data, the baseline FNO model displays an order of magnitude higher prediction errors in regions associated with strong resonances as shown in Fig. 1(c). Furthermore, the model’s effort to fit these extreme resonant responses can lead to overfitting, which reduces prediction accuracy for non-resonant structures

(Section 4 of the Supplementary Information). These behaviors highlight the intrinsic difficulties in EM surrogate solvers due to highly resonant responses.

## 2.2 High-Q Optimization in Traditional Photonics

In conventional photonic design, optimizing high-Q resonant features is intrinsically difficult. The extremely narrow spectral linewidths associated with high-Q modes create sharply peaked, highly nonconvex objective landscapes, making it challenging for optimization algorithms to accurately locate optimal configurations [31,32]. A widely used remedy is to introduce fictitious material absorption during optimization. This artificial loss broadens narrow spectral features, which smooths the overall landscape. From this, it becomes easier to capture the relevant modal behavior, enabling more reliable exploration of the global design space. Once a promising configuration is found, the added loss can be gradually removed, allowing convergence towards the true high-Q response [25-28].

This effect can be understood through the quasinormal mode (QNM) framework. QNMs—solutions to the sourceless Maxwell equations—define the resonant modes of an EM system. QNMs of a system consist of eigenmodes  $\tilde{\mathbf{E}}_m$  and corresponding eigenfrequencies  $\tilde{\omega}_m$ . Such eigenfrequencies are often mentioned as poles, as they are found as the divergent poles of the system for a certain physical response in the complex frequency plane [11]. Now, given a structure with permittivity distribution  $\epsilon(\mathbf{r})$ , adding a small imaginary component  $i\delta\epsilon(\mathbf{r})$  shifts the QNM poles deeper into the complex frequency plane while leaving the real frequency component essentially unchanged. First-order perturbation theory yields a purely imaginary eigenfrequency correction as below [28].

$$\delta\tilde{\omega}_m = -i \frac{\tilde{\omega}_m \int \tilde{\mathbf{E}}_m^* \cdot \delta\epsilon(\mathbf{r}) \tilde{\mathbf{E}}_m d\nu}{2 \int \tilde{\mathbf{E}}_m^* \cdot \epsilon(\mathbf{r}) \tilde{\mathbf{E}}_m d\nu}$$

Such small losses leave the modal field profiles largely intact and don't shift the resonant frequency, but increase the imaginary part of the frequency, which contributes to effective damping of the resonant mode amplitudes (see Section 2 of the Supplementary Information for detailed derivation).

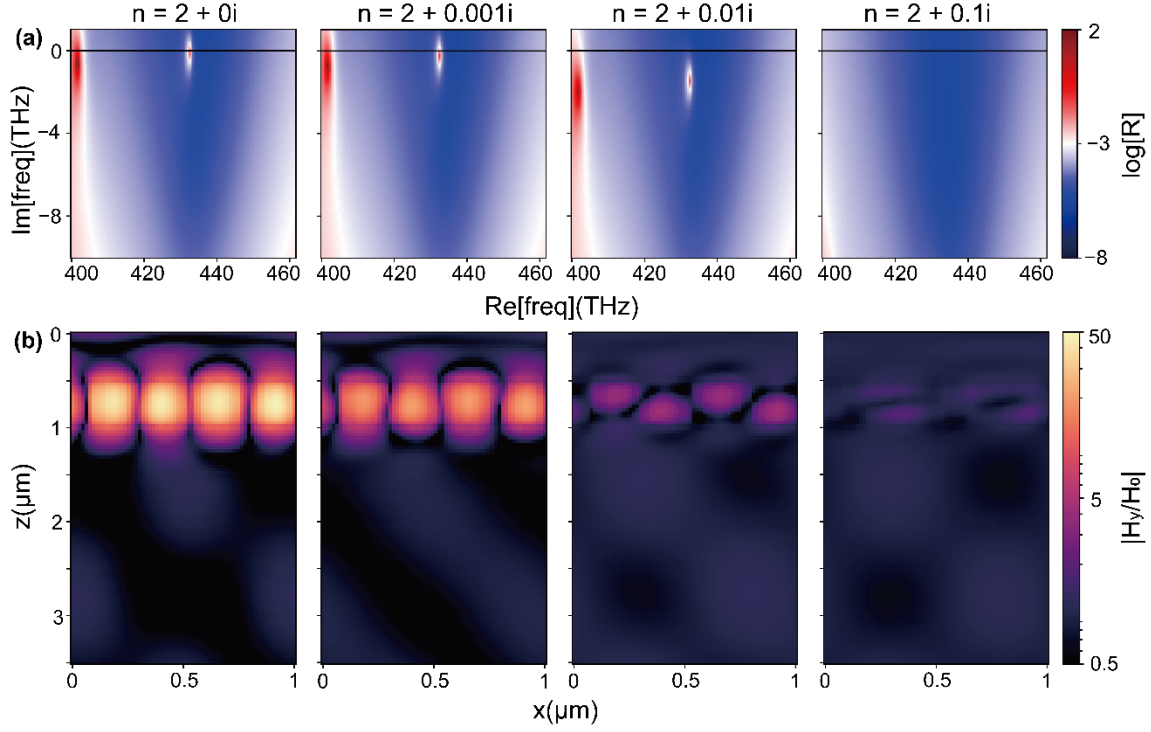


**Figure 2 Relaxation of resonant structures via fictitious material loss.** (a) Complex-frequency sweep of device reflectivity. Introducing a small imaginary component to the refractive index shifts the resonance pole near  $\sim 429$  THz ( $\approx 700$  nm) deeper into the complex-frequency plane. The shift occurs almost entirely along the imaginary axis, indicating increased damping while leaving the real resonance frequency essentially unchanged. (b) Corresponding field distributions at 700 nm. Adding controlled material absorption attenuates the resonant field intensity within the grating region while preserving the underlying modal profile. Among the tested values,  $n = 2 + 0.01i$  provides the most effective balance between amplitude reduction and mode-shape fidelity (see Section 5 of Supplementary Information).

### 2.3 Physics-Inspired Transfer Learning Strategy

The same effect can be applied in our electromagnetic surrogate-model training domain. Certain device configurations exhibit strong guided-mode resonances, generating outlier samples in both training and test datasets. Introducing fictitious absorption—implemented as an additional dielectric loss term—shifts the corresponding QNMs along the imaginary axis, as illustrated in Fig. 2(a). Following the QNM shift, we see a reduction in amplitudes, which is illustrated in Fig. 2(b).

Borrowing the idea of relaxing resonant field intensities to promote more global optimization behavior, we apply a similar strategy to neural network training. Specifically, we aim to guide the model toward learning the general modal contributions first, rather than exposing it to the difficult training landscape, including highly resonant cases. For this, we first train the model using data generated with artificial material loss, or in other words,

lossy data. This initial stage suppresses sharp resonances and helps the model capture the smoother global response landscape. The pre-trained model is then transferred and fine-tuned on the target dataset, which is generated without material loss (lossless) and includes the highly resonant configurations. We name this process dissipative relaxation transfer learning, or DIRT.

For our specific 1D binary grating example, we introduced a small dissipative term to the refractive index ( $n = 2 + 0.01i$ ) chosen to achieve effective amplitude attenuation while preserving the overall modal profiles. The value  $0.01i$  added was shown to be most effective among several test values (see Section 5 of Supplementary Information). In the baseline configuration, where the model was trained solely on lossless data, 9,000 random structures were used, with field data sampled at each wavelength point (9,000 samples  $\times$  11 wavelength points = 99,000 training and test samples). In the DIRT setup, we used 4,500 random structures for both the pretraining (lossy) and fine-tuning (lossless) stages, ensuring that the total amount of training data was equivalent to that of the baseline (49,500 training samples for each stage). The validation and test set consisted of 1,000 random structures generated under lossless conditions, using the same wavelength sampling (11,000 validation and test samples).

We first perform fine-tuning directly from the pretrained model with all parameters unfrozen, which we refer to as l-DIRT, with l standing for loose. In this case, both the pretraining and fine-tuning stages are conducted using the same 10-layer FNO architecture. However, such an approach can lead to forgetting of the pretrained representations. To mitigate this issue, we introduce f-DIRT, with f standing for freeze, where a smaller 6-layer FNO is first pretrained on the lossy dataset, and its parameters are subsequently transferred to a larger 10-layer FNO. The transferred layers are frozen to preserve the learned global features, while the additional deeper layers are trained to capture high-amplitude resonant characteristics. For a fair comparison, the baseline, l-DIRT, and f-DIRT models all share the same final network architecture. The f-DIRT FNO schematic is shown in Fig 3.

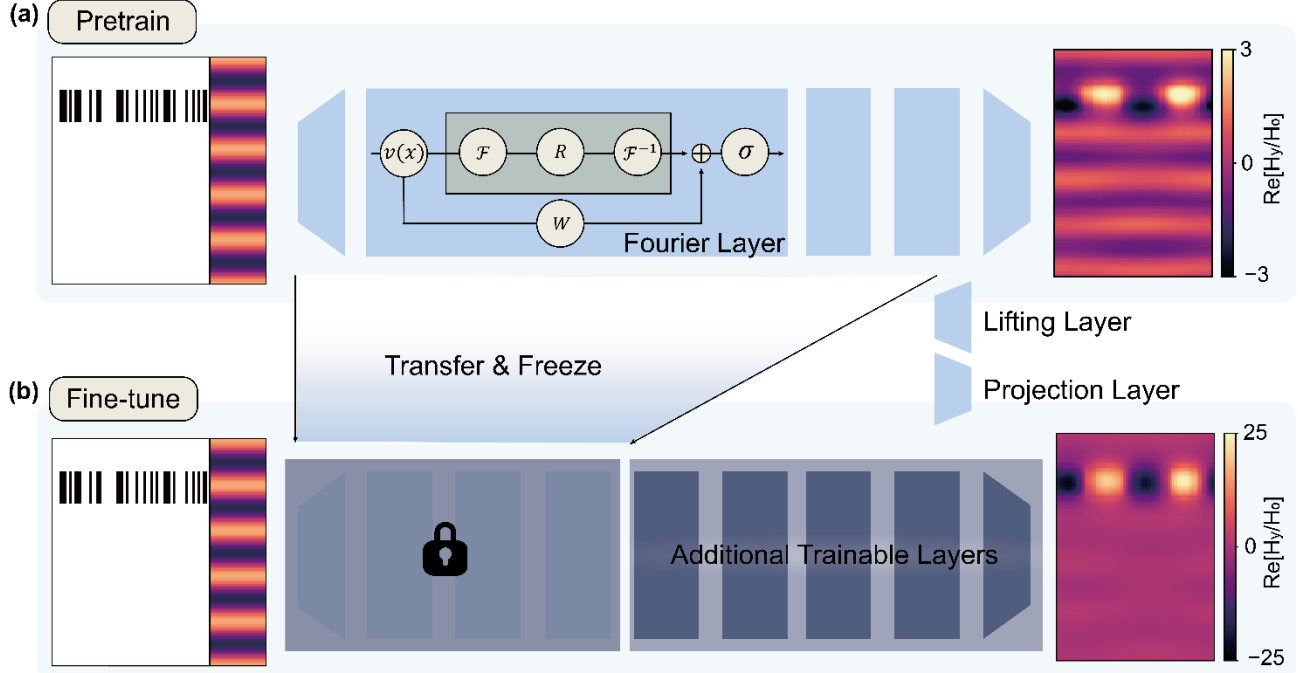


**Figure 3 f-DIRTL FNO training strategy.** (a) Pretraining stage. A 6-layer Fourier Neural Operator (FNO) is trained using structures paired with a wave-prior encoding, which provides both wavelength information and a physically informed ansatz. The pretraining targets are field distributions computed with a small fictitious material loss, resulting in smoothed, attenuated resonances. (b) Fine-tuning stage. The final 10-layer FNO is initialized by transferring and freezing the lifting layer and first six Fourier layers from the pretrained model. The remaining Fourier layers and the projection layer are then trained on the target lossless dataset, which includes high-Q resonant responses.

In the case of UNet, both the freeze and loose variants use identical architectures during pretraining and fine-tuning. For f-DIRTL, only the down-sampling path—the encoder that extracts the underlying physical features—is transferred and frozen during fine-tuning, whereas in l-DIRTL the entire network is updated end-to-end (see Supplementary Section 4). In addition to DIRTL, we also implemented a PINN(physics-informed neural network)-hybrid strategy, implementing Maxwell loss into the training to compare against physics-assisted learning strategies. The Maxwell loss evaluates the degree to which predictions satisfy Maxwell’s equations, thereby providing explicit physical guidance during optimization. Implementation was done by using both MSE and Maxwell loss, with ratio balanced throughout the iterative process (details are provided in Supplementary Section 3). Model performance was evaluated using the normalized prediction error, defined as follows.

$$L_p(\tilde{y}, y) = \frac{1}{N} \sum_{i=1}^N \frac{\|\tilde{y}_i - y_i\|_p}{\|y_i\|_p}$$

### 3. Result and Discussion

#### 3.1 Performance Comparison

**Table 1** Training results for baseline and DIRTl FNO, UNet models

Model	Training Method	Normalized $L_1$ (%)	Normalized $L_2$ (%)
FNO	Baseline	4.80	5.72
	Baseline + PINN	4.50	5.61
	l-DIRTl	4.80	5.78
	f-DIRTl	2.08	2.81
UNet	Baseline	8.11	9.97
	Baseline + PINN	8.15	10.1
	l-DIRTl	7.30	9.16
	f-DIRTl	6.89	8.59

Comparing the f-DIRTl FNO with the baseline FNO reveals a pronounced improvement in prediction accuracy, with the normalized  $L_2$  test error decreasing from 5.72% to 2.81%. As shown in Fig. 4(a), f-DIRTl consistently enhances accuracy across both resonant and non-resonant samples, while Fig. 4(b) shows that, on a per-sample basis, the majority of predictions are more precise than those of the baseline model. Only a very small subset of cases—about 0.4%—exhibits slightly degraded performance, corresponding to highly resonant geometries where both models struggle. This suggests that although f-DIRTl effectively guides the model toward the correct solution manifold, certain resonant cases remain difficult and may warrant further analysis.

Representative field predictions in Fig. 4(c–g) illustrate that f-DIRTl provides lower errors than baseline across multiple wavelengths, improving performance in both resonant conditions (710 nm) and non-resonant cases. In contrast, l-DIRTl does not improve upon the baseline. This outcome indicates that catastrophic forgetting likely occurred during fine-tuning, which diminished the value of the pretrained features. Meanwhile, we employed such a two-step process due to it being most effective, whereas multi-step processes fail due to increase in error during pretrain phases (see Section 6 of Supplementary Information).

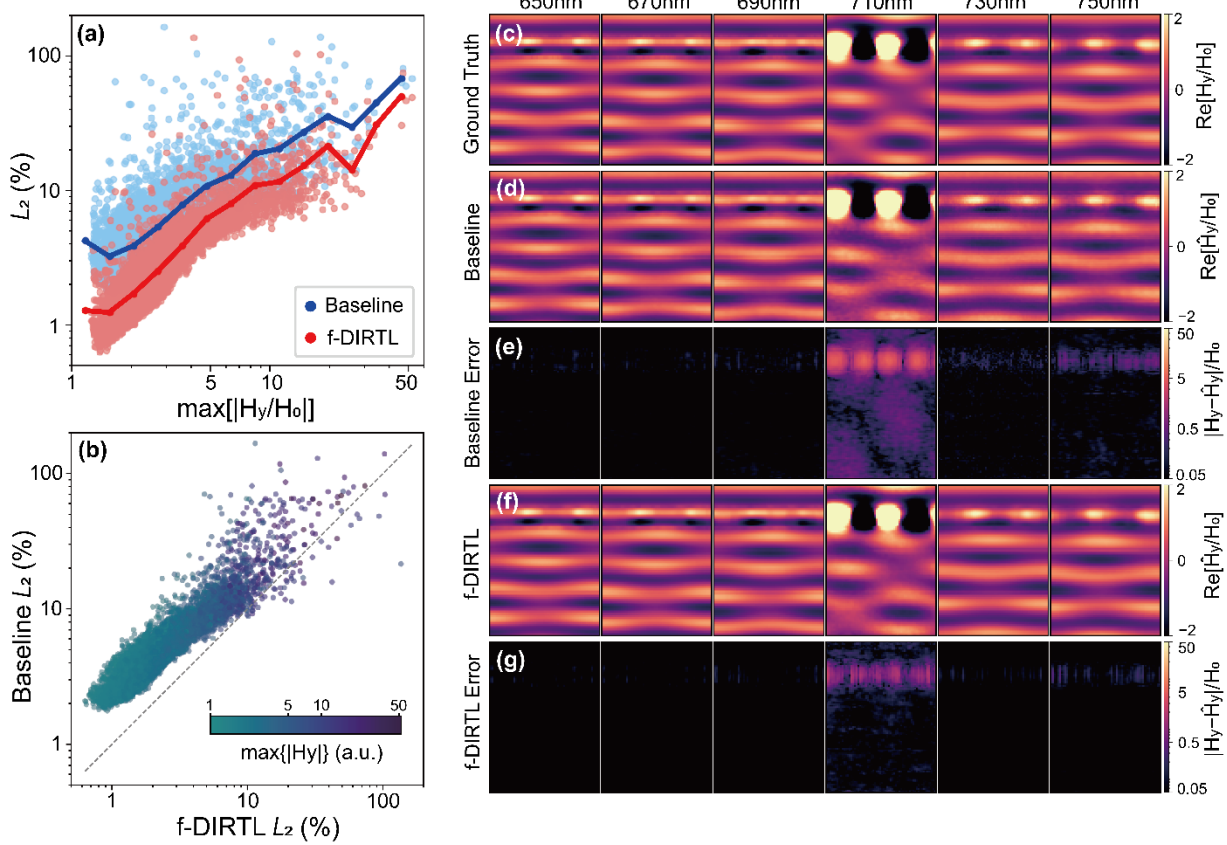


**Figure 4 Comparison test between baseline FNO and f-DIRTL FNO.** Because of the unnoticeable difference between l-DIRTL FNO and baseline FNO, we do not plot results of l-DIRTL FNO (a) Error distribution comparison plot between baseline FNO and f-DIRTL FNO. Each light-blue (baseline FNO) and light-coral (f-DIRTL FNO) point represents the prediction error of an individual test sample plotted against its maximum field amplitude. Blue and red markers show the corresponding average errors within logarithmically spaced amplitude bins for the baseline and f-DIRTL models, respectively. (b) Per-sample error comparison. Each point compares the baseline and f-DIRTL prediction errors for the same sample. Relative to the diagonal  $y = x$ , the strong bias of points toward the baseline-error side indicates that f-DIRTL achieves consistently lower errors across the vast majority of test cases. (c–g) Field distributions and prediction errors for a randomly selected test case at a 20 nm wavelength interval. (c) Ground-truth field distribution. (d) Baseline FNO prediction. (f) f-DIRTL FNO prediction. (e, g) Corresponding prediction-error maps for (e) the baseline FNO and (g) the f-DIRTL FNO. We see that resonance predictions are improved in f-DIRTL FNO.

The benefits of DIRTL are also apparent when trained with UNet architecture. Despite UNet's more limited representational capacity compared to FNO, f-DIRTL UNet still achieves a 1.4% reduction in normalized  $L_2$  error relative to its baseline counterpart. Interestingly, l-DIRTL UNet also delivers measurable improvements, a trend not observed with FNO. This outcome is likely tied to the use of carefully selected learning rates, suggesting that additional fine-tuning may allow similar gains for l-DIRTL FNO. These results underline DIRTL's adaptability across architectures, strengthening its promise as a model-agnostic training strategy.

Meanwhile, for Maxwell loss implemented cases, we also see little improvement ( $\sim 0.1\%$  relative  $L_2$ ) in FNO and no improvement in UNet. This is noted by baseline + PINN in Table 1. Although the Maxwell loss provides some assistance during FNO training, our proposed two-step strategy delivers substantially greater improvements in predictive accuracy. This contrast indicates that the primary challenge in modeling resonant responses does not stem from insufficient physical constraints, but rather from their statistical outlier nature within the dataset. Consequently, achieving accurate predictions in resonant regimes requires explicitly addressing these outlier characteristics in the data distribution, rather than relying solely on physics-based regularization.

### 3.2 Data Efficiency Analysis

The most notable achievement of this approach lies in its ability to achieve substantial performance gains without increasing the total size of the training dataset or changing the model architecture. Even with a smaller quantity of target-task data, the high-accuracy pretrained core effectively steers the model toward the correct solution, enabling more efficient adaptation than relying on target-task data alone. This behavior differs from standard transfer learning examples, which are typically characterized by large-scale pretraining followed by limited fine-tuning [33,34].

To directly assess the data-efficiency advantages of f-DIRTL FNO over the baseline FNO, we trained both models using varying amounts of training data. Specifically, we prepared datasets consisting of 500, 1,000, 3,000, and 9,000 unique structures, each sampled at 11 wavelength points. For f-DIRTL FNO, half of the samples were used for the lossy pretraining stage and the remaining half for fine-tuning. All training runs used identical learning-rate schedulers as in Section 3.1 to ensure fair comparison.

The resulting prediction errors and distributions are summarized in Fig. 5(a). Across all dataset sizes, f-DIRTL FNO consistently outperforms the baseline FNO. Notably, when trained with 9,000 structures, the baseline FNO achieves a normalized  $L_2$  error of 5.72%, which is comparable to the f-DIRTL FNO trained with only 1,000 structures (6.25%). This quantitative comparison suggests that f-DIRTL can achieve similar accuracy with nearly an order of magnitude fewer training samples, corresponding to an effective  $\sim 9$  times improvement in data efficiency. Such a gain significantly enhances the practicality and productivity of neural operator-based EM surrogate solvers.

### 3.3 Robustness Assessment for f-DIRTL

To evaluate the robustness of f-DIRTL FNO to different training conditions, we conducted two hyperparameter sweeps. First, we varied the number of Fourier layers used during pretraining, transferring and freezing 4 to 10 layers into a 10-layer fine-tuned FNO model. Second, we investigated the effect of the pretrain-to-fine-tune data ratio, where a ratio of 0.1 indicates that the pretraining dataset consists of 10% of the total dataset, with the remaining 90% being for fine-tuning. Ratios from 0.1 to 0.9 were tested in increments of 0.1. All experiments used a total of 3,000 randomly sampled structures with wavelengths from 650 nm to 750 nm at 10 nm intervals (3,000 samples  $\times$  11 wavelength points = 33,000 training samples). These sweeps allowed us to assess how f-DIRTL performance depends on both dataset distribution and model design.

In the second hyperparameter sweep, we varied the number of Fourier layers used during pretraining and the number of layers transferred to the fine-tuned model. This enabled us to evaluate how different transfer strategies affect the final prediction accuracy. Adjusting the number of transferred layers also provided insight into how information learned during pretraining is distributed throughout the model. For this study, both the pretraining and transfer stages used 1,500 randomly sampled structures (1,500 samples  $\times$  11 wavelength points = 16,500 training samples for each phase, total 33,000 training samples). We tested pretrained models with 4 to 10 Fourier layers and transferred anywhere from a single layer to the entire sequence.

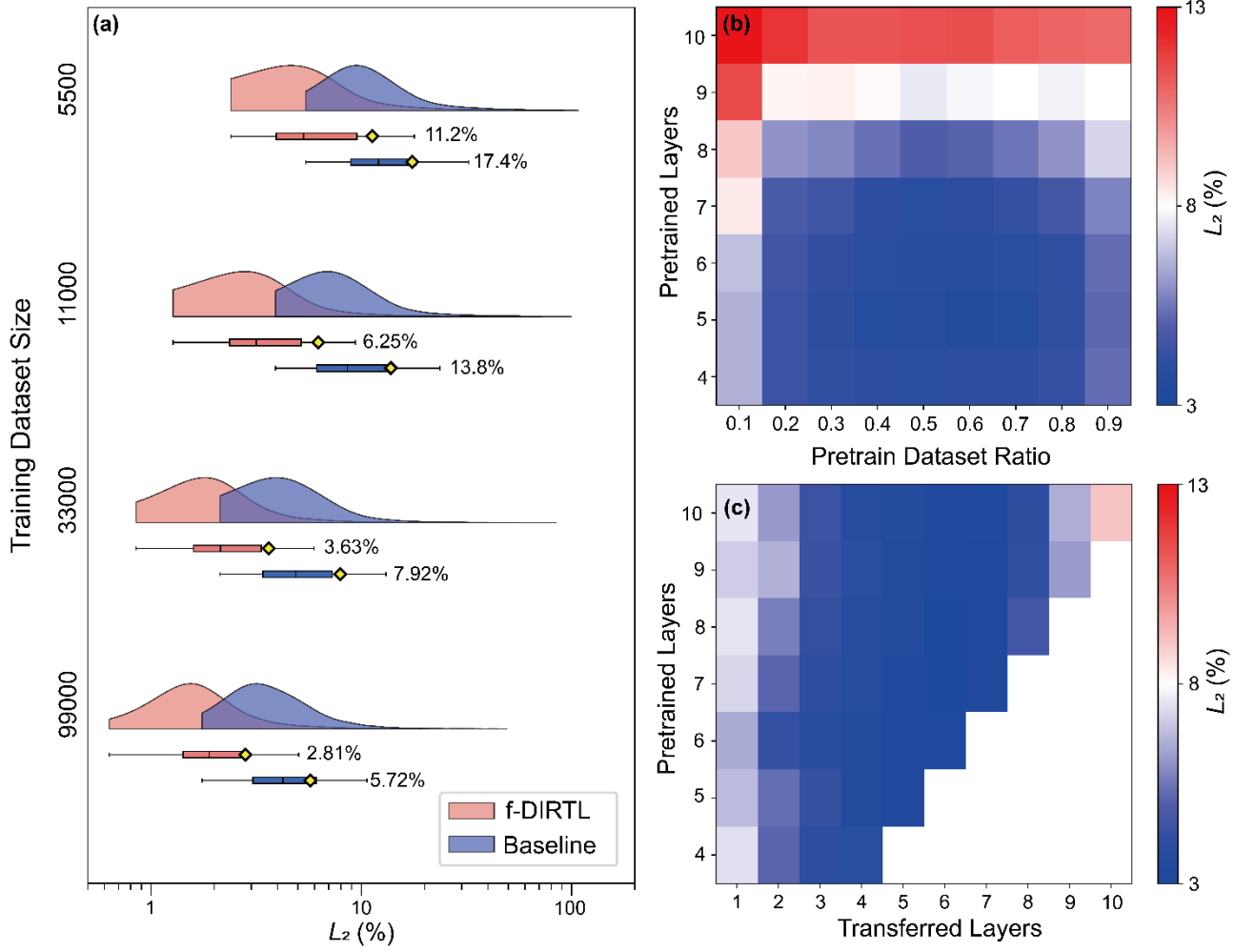


**Figure 5 Robustness test on training dataset size and training condition** (a) Density plot of normalized  $L_2$  errors with varying training set sizes. Density plots show kernel density estimates of the normalized  $L_2$  error distributions for both models across different training-set sizes. Beneath each density curve, horizontal box plots summarize the corresponding distributions, showing the median (notch), quartiles, and whiskers, with yellow diamonds marking the mean values annotated alongside each box. (b) Hyperparameter sweep altering ratio of pretrain dataset and number of Fourier layers used in pretrain stage. (c) Hyperparameter sweep altering number of Fourier layers in pretrain stage and amount of layers transferred in the fine-tune stage. For both (b) and (c), the colormap indicates that shades of blue are better than baseline, and shades or red are worse than baseline.

The results of these sweeps are shown in Fig. 5(b) and (c). In Fig. 5(b), the prediction error increases sharply when pretraining more than eight layers. This is primarily due to underfitting during the fine-tuning stage, as there are too few trainable parameters remaining. In contrast, pretraining and transferring fewer than eight layers results in a model that is robust to dataset distribution, with prediction errors around or below 4%, with the best case reaching 3.6% (baseline FNO error for 3k random structures is 7.9%). This behavior reflects a simple trade-off: using more data for pretraining improves the accuracy of the pretrained core, while having sufficient data in fine-

tuning ensures accurate adaptation. This test suggests that, when applying this strategy, the dataset can be prepared without excessive concern for data balance, provided that the pretrain and fine-tune dataset sizes are roughly comparable.

In Fig. 5(c), we observe that, regardless of the total number of pretrained layers, transferring between four and seven layers yields the best results. For larger pretrained models, partially transferring the network allows the fine-tuned model to retain sufficient trainable parameters for adapting to the target problem. Conversely, for smaller pretrained models, transferring nearly all pretrained layers produced the best performance, suggesting that most of the learned physical information is in the deeper Fourier layers. Nevertheless, even transferring just one or two layers improves fine-tuned accuracy beyond the baseline, indicating that essential physical features are also embedded within the lower layers of the network.

Meanwhile, both the f-DIRTL FNO and the baseline FNO exhibit excellent interpolation performance at unseen wavelengths, demonstrating robust inference capability. This inference ability is further enhanced during the lossy pretraining phase, where the pretrained model demonstrates interpolation over broader wavelength ranges as well as wavelength extrapolation. These results are directly utilized as multi-tasking of the DIRTL framework, in which a coarsely trained pretrained core is effectively adapted to more specific target tasks during the fine-tuning phase. Details on this are demonstrated in Section 7 of Supplementary Information.

## 4. Conclusion

In this work, we introduced dissipative relaxation transfer learning (DIRTL), a physics-inspired training strategy designed to resolve a central challenge in electromagnetic surrogate modeling: accurately learning high-amplitude resonant responses that appear as statistical outliers within predominantly non-resonant datasets. Drawing an analogy to loss-regularized optimization in photonic design, DIRTl employs a two-stage curriculum in which resonant features are first attenuated using fictitious material absorption and are later reintroduced during fine-tuning. This process enables the model to first acquire a smooth, global modal structure before confronting the sharp, nonconvex characteristics of high-Q responses.

Our experimental results show that DIRTl significantly improves surrogate-solver accuracy, whilst preserving the total amount of training data required. In particular, the f-DIRTl variant—where pretrained layers are transferred and frozen within a deeper fine-tuning model—achieves more than a twofold reduction in prediction error compared with baseline FNO training. In addition, our dataset-scaling experiments show that the f-DIRTl FNO achieves comparable prediction accuracy using only about one-ninth of the total training data required by the baseline model. Such results are uncommon in conventional transfer learning, underscoring the pretrained core’s ability to provide physically meaningful guidance.

Comprehensive parameter sweeps further show that DIRTl retains strong performance across diverse dataset splits and transfer configurations, highlighting both its robustness and its ease of integration into existing workflows. In particular, experiments varying the number of transferred Fourier layers demonstrate that most of the physically meaningful representations are preserved when the entire sequence of pretrained layers is transferred. Nevertheless, even transferring only one or two layers yields improvements over the baseline, suggesting that essential physical features are also encoded in the shallow layers. Across architectures, consistent gains are observed for both FNO and UNet, confirming that DIRTl is fundamentally model-agnostic, relying on the structure of the data curriculum rather than architecture-specific design.

Taken together, these results establish DIRTl as a data-efficient and physically informed framework that integrates principles from photonic optimization into transfer learning. The method illustrates how a strategically structured training curriculum can guide a neural network toward learning the underlying physics with minimal

data. Given its model-agnostic nature and demonstrated robustness, DIRT holds strong potential for broad applicability—not only in electromagnetic surrogate modeling but across a wide class of physical systems where physics-informed learning is essential.

## **Acknowledgements**

This work was supported by the Culture, Sports and Tourism R&D Program through the Korea Creative Content Agency (KOCCA), funded by the Ministry of Culture, Sports and Tourism (RS-2024-00332210), and by the National Research Foundation of Korea (NRF) grants funded by the Ministry of Science and ICT (RS-2024-00414119 and RS-2024-00416583) and the Ministry of Education (RS-2024-00360139), Republic of Korea.

## References

[1] Hafiz, A. M., Faiq, I., & Hassaballah, M. (2024). Solving partial differential equations using large-data models: a literature review. *Artificial Intelligence Review*, 57(6), 152.

[2] Jiang, J., Chen, M., & Fan, J. A. (2021). Deep neural networks for the evaluation and design of photonic devices. *Nature Reviews Materials*, 6(8), 679-700.

[3] Park, J., Kim, S., Nam, D. W., Chung, H., Park, C. Y., & Jang, M. S. (2022). Free-form optimization of nanophotonic devices: from classical methods to deep learning. *Nanophotonics*, 11(9), 1809-1845.

[4] Ma, X., Ma, Y., Cunha, P., Liu, Q., Kudtarkar, K., Xu, D., ... & Lan, S. (2021). A universal deep learning strategy for designing high-quality-factor photonic resonances. *arXiv preprint arXiv:2105.03001*.

[5] Mao, C., Lupoiu, R., Dai, T., Chen, M., & Fan, J. A. (2024). Towards general neural surrogate solvers with specialized neural accelerators. *arXiv preprint arXiv:2405.02351*.

[6] Seo, J., Kang, C., Seo, D., & Chung, H. (2024). Wave interpolation neural operator: Interpolated prediction of electric fields across untrained wavelengths. In *NeurIPS 2024 Workshop on Data-driven and Differentiable Simulations, Surrogates, and Solvers*.

[7] Asano, T., & Noda, S. (2018). Optimization of photonic crystal nanocavities based on deep learning. *Optics express*, 26 (25), 32704-32717.

[8] Wiecha, P. R., & Muskens, O. L. (2019). Deep learning meets nanophotonics: a generalized accurate predictor for near fields and far fields of arbitrary 3D nanostructures. *Nano letters*, 20 (1), 329-338.

[9] Duarte, D. H. G., De Lima, P. D. S., & De Araújo, J. M. (2025). Outlier-resistant physics-informed neural network. *Physical Review E*, 111(2), L023302.

[10] Okuno, A., & Yagishita, S. (2023). Outlier-robust neural network training: Efficient optimization of transformed trimmed loss with variation regularization. *arXiv preprint arXiv:2308.02293*.

[11] Lalanne, P., Yan, W., Vynck, K., Sauvan, C., & Hugonin, J. P. (2018). Light interaction with photonic and plasmonic resonances. *Laser & Photonics Reviews*, 12(5), 1700113.

[12] Soljačić, M., & Joannopoulos, J. D. (2004). Enhancement of nonlinear effects using photonic crystals. *Nature materials*, 3(4), 211-219.

[13] Lu, L., Jin, P., Pang, G., Zhang, Z., & Karniadakis, G. E. (2021). Learning nonlinear operators via DeepONet based on the universal approximation theorem of operators. *Nature machine intelligence*, 3(3), 218-229.

[14] Ma, Q., Jiang, X., Guo, X., Zhou, Q., Wang, X., Yu, H., & Ni, K. (2025). Layer-Interaction DeepONet for modeling ultrafast nonlinear dynamics in optical fibers. *Journal of Lightwave Technology*.

[15] Krizhevsky, A., Sutskever, I., & Hinton, G. E. (2012). Imagenet classification with deep convolutional neural networks. *Advances in neural information processing systems*, 25.

[16] Chen, M., Lupoiu, R., Mao, C., Huang, D. H., Jiang, J., Lalanne, P., & Fan, J. A. (2022). High-speed simulation and freeform optimization of nanophotonic devices with physics-augmented deep learning. *ACS Photonics*, 9(9), 3110-3123.

[17] Zhu, L., Lv, C., Hua, W., Huang, D., & Liu, Y. (2025). PTLOR-Net: Physical Transfer Learning Based Optical Response Prediction Network of Metasurfaces. *ACS Photonics*, 12(5), 2624-2636.

[18] Lim, J., & Psaltis, D. (2022). MaxwellNet: Physics-driven deep neural network training based on Maxwell's equations. *Apl Photonics*, 7(1).

[19] Lynch, S., LaMountain, J., Fan, B., Bu, J., Raju, A., Wasserman, D., ... & Podolskiy, V. A. (2025). Physics-Guided Hierarchical Neural Networks for Maxwell's Equations in Plasmonic Metamaterials. *ACS photonics*, 12(8), 4279-4288.

[20] Khan, M. R., Zekios, C. L., Bhardwaj, S., & Georgakopoulos, S. V. (2024). A deep learning convolutional neural network for antenna near-field prediction and surrogate modeling. *IEEE Access*, 12, 39737-39747.

[21] Park, C., Kim, S., Jung, A. W., Park, J., Seo, D., Kim, Y., ... & Jang, M. S. (2024). Sample-efficient inverse design of freeform nanophotonic devices with physics-informed reinforcement learning. *Nanophotonics*, 13(8), 1483-1492.

[22] Li, Z., Kovachki, N., Azizzadenesheli, K., Liu, B., Bhattacharya, K., Stuart, A., & Anandkumar, A. (2020). Fourier neural operator for parametric partial differential equations. *arXiv preprint arXiv:2010.08895*.

[23] Gu, J., Gao, Z., Feng, C., Zhu, H., Chen, R., Boning, D., & Pan, D. (2022). Neurolight: A physics-agnostic neural operator enabling parametric photonic device simulation. *Advances in Neural Information Processing Systems*, 35, 14623-14636.

[24] Augenstein, Y., Repan, T., & Rockstuhl, C. (2023). Neural operator-based surrogate solver for free-form electromagnetic inverse design. *ACS Photonics*, 10(5), 1547-1557.

[25] Liang, X., & Johnson, S. G. (2013). Formulation for scalable optimization of microcavities via the frequency-averaged local density of states. *Optics express*, 21(25), 30812-30841.

[26] Jin, W., Li, W., Orenstein, M., & Fan, S. (2020). Inverse design of lightweight broadband reflector for relativistic lightsail propulsion. *ACS Photonics*, 7(9), 2350-2355.

[27] Yao, W., Verdugo, F., Christiansen, R. E., & Johnson, S. G. (2022). Trace formulation for photonic inverse design with incoherent sources. *Structural and Multidisciplinary Optimization*, 65(11), 336.

[28] Granchi, N., Intonti, F., Florescu, M., García, P. D., Gurioli, M., & Arregui, G. (2023). Q-factor optimization of modes in ordered and disordered photonic systems using non-Hermitian perturbation theory. *ACS photonics*, 10(8), 2808-2815.

[29] Kim, Y., Jung, A. W., Kim, S., Octavian, K., Heo, D., Park, C., ... & Park, C. Y. (2024). Meent: Differentiable electromagnetic simulator for machine learning. *arXiv preprint arXiv:2406.12904*.

[30] Kingma, D. P. (2014). Adam: A method for stochastic optimization. *arXiv preprint arXiv:1412.6980*.

[31] Deng, R., Liu, W., & Shi, L. (2024). Inverse design in photonic crystals. *Nanophotonics*, 13(8), 1219-1237.

[32] Ahn, G. H., Yang, K. Y., Trivedi, R., White, A. D., Su, L., Skarda, J., & Vuckovic, J. (2022). Photonic inverse design of on-chip microresonators. *ACS Photonics*, 9(6), 1875-1881.

[33] Shin, J. M., Kim, S., Menabde, S. G., Park, S., Lee, I. G., Kim, I., & Jang, M. S. (2025). Data-efficient prediction of OLED optical properties enabled by transfer learning. *Nanophotonics*, 14(8), 1091-1099.

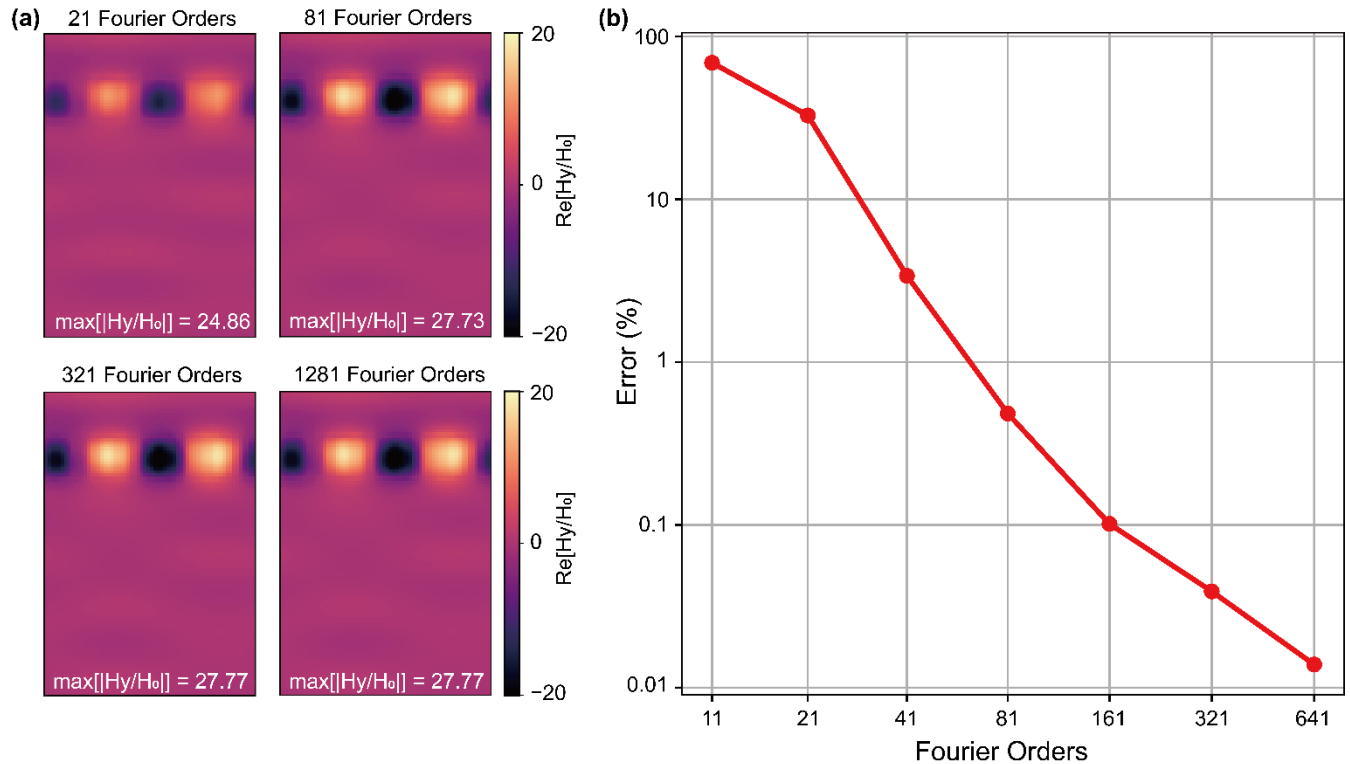
[34] Pan, S. J., & Yang, Q. (2009). A survey on transfer learning. *IEEE Transactions on knowledge and data engineering*, 22(10), 1345-1359.

## Supplementary Information

### S1. RCWA Engine Convergence Test

To generate the training and test datasets used for neural operator training, we employed the `meent` RCWA engine [1]. The selection of the Fourier order was determined through a convergence study conducted on a highly resonant test structure. We first generated 1,000 random structural samples at 700 nm using a high reference setting of 101 Fourier orders, and identified a structure exhibiting strong resonance. Using this structure, we evaluated the field convergence across varying Fourier orders. Convergence was evaluated by comparing the results obtained at each Fourier order with those computed using a very high reference setting of 1281 Fourier orders. Error rate was measured using normalized  $L_2$  error.

From this analysis, 81 Fourier orders were found to provide a suitable balance between numerical accuracy and computational efficiency for large-scale dataset generation, retaining below 1% normalized  $L_2$  error. The simulation results are shown in Supplementary Fig. 1(a), whilst the error for each Fourier order is shown in Supplementary Fig. 1(b).



**Supplementary Figure 1** Convergence test for RCWA engine under various Fourier orders. Bottom right result shows that for FEM solver.

## S2. Quasinormal Mode Decomposition of Field Response

The resonant modes of an electromagnetic system can be obtained by solving a sourceless Maxwell wave equation, which forms an eigenvalue problem for the electric field. These eigenmodes are characterized by complex frequency eigenvalues, known as resonant frequencies or quasinormal modes (QNMs) [2]. Formally, for systems with free-space magnetic permeability  $\mu_0$ , the electromagnetic problem can be expressed as

$$\frac{1}{\mu_0} \nabla \times \nabla \times \mathbf{E} - \omega^2 \epsilon(\mathbf{r}) \mathbf{E} = i\omega \mathbf{J}(\mathbf{r})$$

The corresponding sourceless eigenproblem defining QNMs is then given as

$$\nabla \times \nabla \times \tilde{\mathbf{E}}_m = \left( \frac{\tilde{\omega}_m}{c} \right)^2 \epsilon(\mathbf{r}) \tilde{\mathbf{E}}_m, \quad \epsilon(\mathbf{r}) = \epsilon_0 \epsilon(\mathbf{r})$$

where  $\tilde{\mathbf{E}}_m$  and  $\tilde{\omega}_m$  denote the  $m$ th quasinormal mode and its corresponding complex eigenfrequency. In practice, these modes can be computed using eigenfrequency solvers or complex-frequency sweeps. For example, using the S4 RCWA solver that supports complex frequency analysis, the reflection spectrum reveals a pole near 700 nm, slightly below the real axis in the complex frequency plane (see Fig. 2(a)), corresponding to a resonant QNM [3].

Now, to study the effect of small material absorption, we introduce a small complex permittivity term  $i\delta\epsilon(r)$  to the system, which can be written in a perturbed eigenproblem like below.

$$\nabla \times \nabla \times (\tilde{\mathbf{E}}_m + \delta\tilde{\mathbf{E}}_m) = \left( \frac{\tilde{\omega}_m + \delta\tilde{\omega}_m}{c} \right)^2 (\epsilon(\mathbf{r}) + i\delta\epsilon(\mathbf{r})) (\tilde{\mathbf{E}}_m + \delta\tilde{\mathbf{E}}_m)$$

Retaining only first-order perturbation terms, we have

$$\nabla \times \nabla \times \delta\tilde{\mathbf{E}}_m = i \left( \frac{\tilde{\omega}_m}{c} \right)^2 \delta\epsilon(\mathbf{r}) \tilde{\mathbf{E}}_m + \left( \frac{\tilde{\omega}_m}{c} \right)^2 \epsilon(\mathbf{r}) \delta\tilde{\mathbf{E}}_m + 2 \left( \frac{\tilde{\omega}_m}{c^2} \right) \delta\tilde{\omega}_m \epsilon(\mathbf{r}) \tilde{\mathbf{E}}_m$$

Now, as the new eigenmode  $\tilde{\mathbf{E}}_m + \delta\tilde{\mathbf{E}}_m$  can be described as a span of quasinormal modes;  $\tilde{\mathbf{E}}_m + \delta\tilde{\mathbf{E}}_m = \sum_n \alpha_n \tilde{\mathbf{E}}_n$ , we can describe the correction term as span of eigenmodes not including original  $m^{\text{th}}$  eigenmode [4]. Therefore, utilizing the orthonormality of quasinormal modes

$$\delta\tilde{\mathbf{E}}_m = \sum_{n \neq m} \alpha_n \tilde{\mathbf{E}}_n, \quad \int \tilde{\mathbf{E}}_m^* \cdot \tilde{\mathbf{E}}_n d\mathbf{v} = \delta_{mn}$$

Taking inner product for first order equation with  $\tilde{\mathbf{E}}_m^*$ , we get

$$i \left( \frac{\tilde{\omega}_m}{c} \right)^2 \int \tilde{\mathbf{E}}_m^* \cdot \delta\epsilon(\mathbf{r}) \tilde{\mathbf{E}}_m d\nu = -2 \left( \frac{\tilde{\omega}_m}{c^2} \right) \delta\tilde{\omega}_m \int \tilde{\mathbf{E}}_m^* \cdot \epsilon(\mathbf{r}) \tilde{\mathbf{E}}_m d\nu$$

From this, we get the well known first-order correction for eigenfrequency  $\delta\tilde{\omega}_m$ .

$$\delta\tilde{\omega}_m = -i \frac{\tilde{\omega}_m \int \tilde{\mathbf{E}}_m^* \cdot \delta\epsilon(\mathbf{r}) \tilde{\mathbf{E}}_m d\nu}{2 \int \tilde{\mathbf{E}}_m^* \cdot \epsilon(\mathbf{r}) \tilde{\mathbf{E}}_m d\nu}$$

Hence, the perturbation  $i\delta\epsilon(\mathbf{r})$  contributes only to the imaginary part of the eigenfrequency, confirming that small fictitious loss affects resonance linewidth, but not the real resonance position. This effect is well shown in the pole shift in Fig. 2(a).

Now, for the mode correction terms, substituting  $\delta\tilde{\mathbf{E}}_m = \sum_{n \neq m} \alpha_n \tilde{\mathbf{E}}_n$  to first order perturbation equation, we obtain

$$\sum_{n \neq m} \alpha_n \nabla \times \nabla \times \tilde{\mathbf{E}}_n = i \left( \frac{\tilde{\omega}_m}{c} \right)^2 \delta\epsilon(\mathbf{r}) \tilde{\mathbf{E}}_m + \left( \frac{\tilde{\omega}_m}{c} \right)^2 \epsilon(\mathbf{r}) \sum_{n \neq m} \alpha_n \tilde{\mathbf{E}}_n + 2 \left( \frac{\tilde{\omega}_m}{c^2} \right) \delta\tilde{\omega}_m \epsilon(\mathbf{r}) \tilde{\mathbf{E}}_m$$

As  $\nabla \times \nabla \times \tilde{\mathbf{E}}_n = \left( \frac{\tilde{\omega}_n}{c} \right)^2 \epsilon(\mathbf{r}) \tilde{\mathbf{E}}_n$ , we can rewrite as

$$\sum_{n \neq m} \alpha_n \left( \frac{\tilde{\omega}_n^2 - \tilde{\omega}_m^2}{c^2} \right) \epsilon(\mathbf{r}) \tilde{\mathbf{E}}_n = i \left( \frac{\tilde{\omega}_m}{c} \right)^2 \delta\epsilon(\mathbf{r}) \tilde{\mathbf{E}}_m + 2 \left( \frac{\tilde{\omega}_m}{c^2} \right) \delta\tilde{\omega}_m \epsilon(\mathbf{r}) \tilde{\mathbf{E}}_m$$

Now, taking inner product with  $\tilde{\mathbf{E}}_n^*$ , we get

$$\begin{aligned} \alpha_n \left( \frac{\tilde{\omega}_n^2 - \tilde{\omega}_m^2}{c^2} \right) \epsilon(\mathbf{r}) &= i \left( \frac{\tilde{\omega}_m}{c} \right)^2 \int \tilde{\mathbf{E}}_n^* \cdot \delta\epsilon(\mathbf{r}) \tilde{\mathbf{E}}_m d\nu \\ \alpha_n &= \frac{i \tilde{\omega}_m^2 \int \tilde{\mathbf{E}}_n^* \cdot \delta\epsilon(\mathbf{r}) \tilde{\mathbf{E}}_m d\nu}{(\tilde{\omega}_n^2 - \tilde{\omega}_m^2) \epsilon(\mathbf{r})} \\ \delta\tilde{\mathbf{E}}_m &= i \sum_{n \neq m} \frac{\tilde{\omega}_m^2 \int \tilde{\mathbf{E}}_n^* \cdot \delta\epsilon(\mathbf{r}) \tilde{\mathbf{E}}_m d\nu}{(\tilde{\omega}_n^2 - \tilde{\omega}_m^2) \epsilon(\mathbf{r})} \tilde{\mathbf{E}}_n \end{aligned}$$

By this, we can also derive the mode correction term via first order perturbation. Meanwhile, now approaching the Maxwell equation in terms of Green's function like below,

$$\frac{1}{\mu_0} \nabla \times \nabla \times G(\mathbf{r}, \mathbf{r}', \omega) - \omega^2 \epsilon(\mathbf{r}) G(\mathbf{r}, \mathbf{r}', \omega) = \mathbf{I} \delta(\mathbf{r} - \mathbf{r}')$$

we can decompose the Green's function via quasinormal modes like below [2]

$$G(\mathbf{r}, \mathbf{r}', \omega) = - \sum_m \frac{\tilde{\mathbf{E}}_m(\mathbf{r}) \otimes \tilde{\mathbf{E}}_m(\mathbf{r}')}{\omega(\omega - \tilde{\omega}_m)}$$

which yields the field response

$$E(r) = \int G(\mathbf{r}, \mathbf{r}', \omega) \cdot i\omega \mathbf{J}(\mathbf{r}) d\nu' = -i \sum_m \int \frac{\tilde{\mathbf{E}}_m(\mathbf{r}) \otimes \tilde{\mathbf{E}}_m(\mathbf{r}')}{\omega(\omega - \tilde{\omega}_m)} \cdot \mathbf{J}(\mathbf{r}) d\nu'$$

For non-resonant structures, the quasinormal mode (QNM) poles are located far from the real frequency axis. Consequently, the term  $\omega - \tilde{\omega}_m$  remains large, resulting in weak field amplitudes and minimal energy localization. In contrast, high-Q resonant structures exhibit poles that lie close to the real axis. In this case, at real frequency  $\omega = \text{Re}\{\tilde{\omega}_m\}$ , the term  $\omega - \tilde{\omega}_m$  becomes notably small, leading to pronounced field localization and significant amplitude enhancement due to emphasis on mth resonant mode.

Introducing a small fictitious loss alters this behavior in a controlled manner. The additional absorption increases the imaginary part of the complex frequency  $\tilde{\omega}_m$ , effectively enlarging the denominator of Green's function and thereby reducing the field amplitude near resonance. Importantly, because both the frequency and modal corrections are first-order in the perturbation, such a small absorption term (on the order of 1%) primarily suppresses amplitude growth while preserving the mode shape and the real part of the resonant frequency.

Altogether, this analysis provides a quantitative foundation for the loss-regularization strategy. It explains how the deliberate introduction of minor absorption smoothens the learning field involving high-Q resonances, effectively attenuating the high modal amplitudes without compromising the physical fidelity of the underlying modal characteristics and the position of resonant frequency.

### S3. Addition of Maxwell Loss

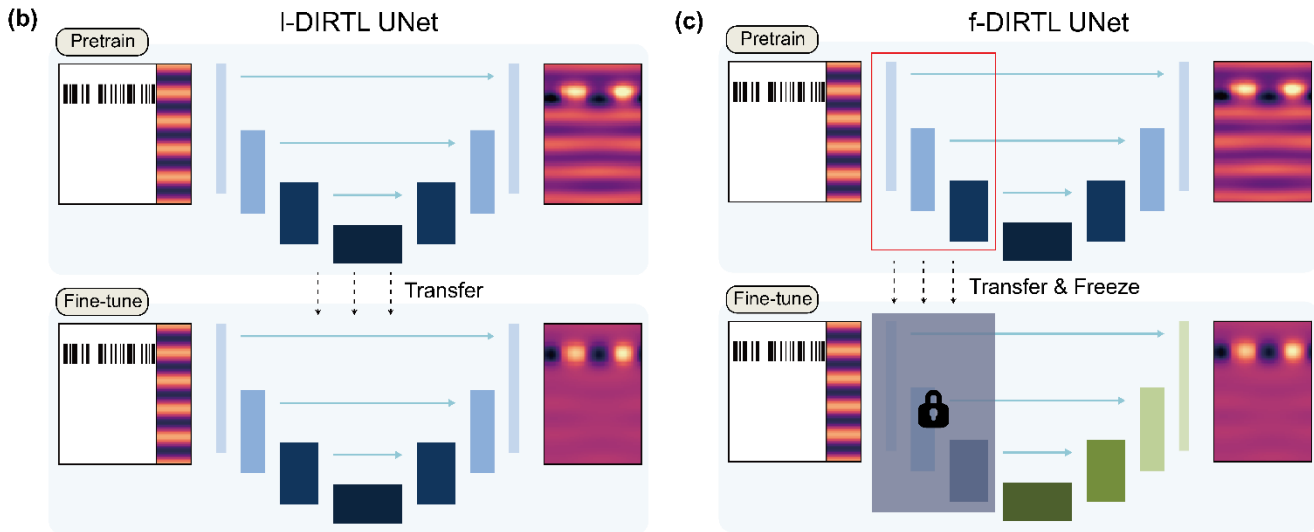
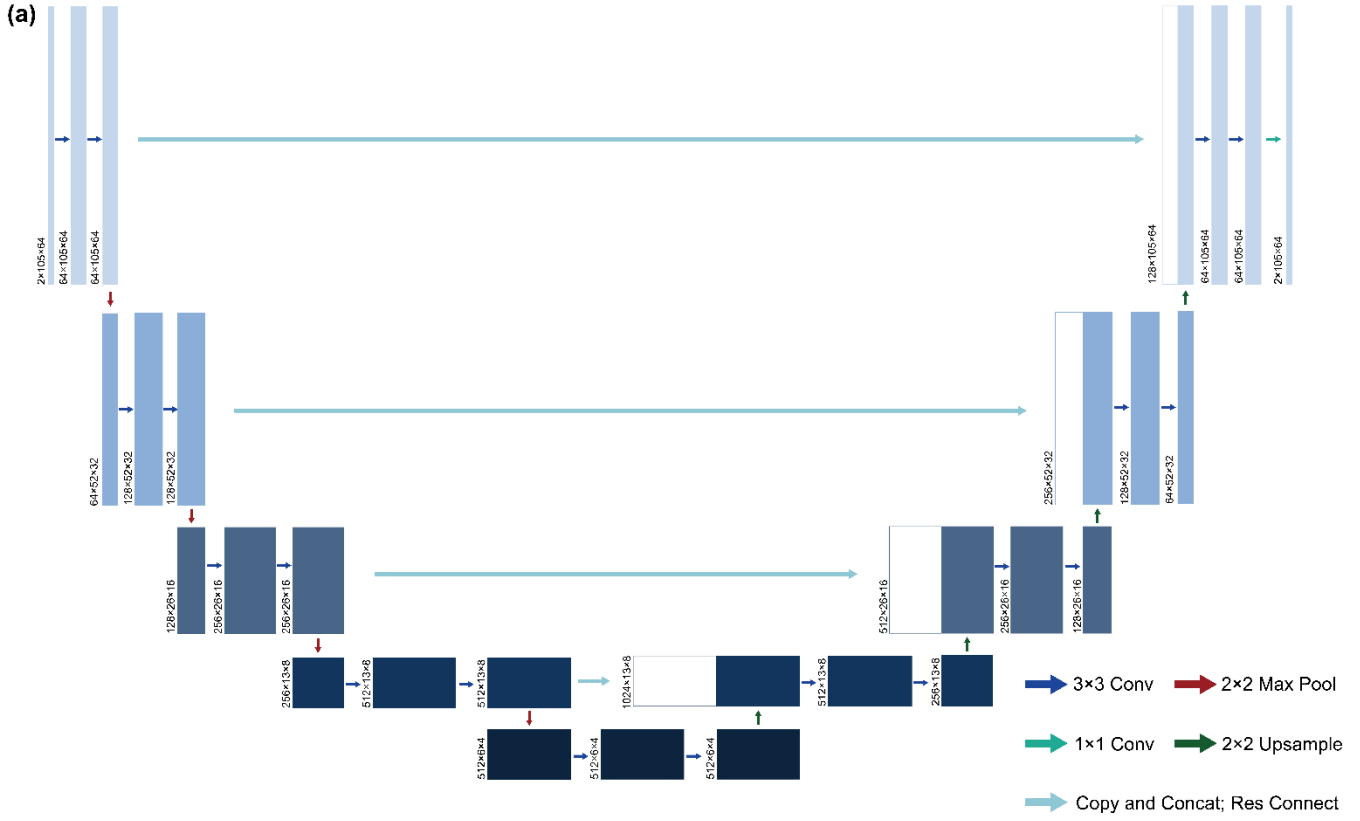
The balance between physical Maxwell loss and MSE data loss was controlled by hyperparameter  $\alpha$ , which scales the Maxwell loss term like below.

$$L = L_{\text{MSE}} + \alpha \cdot L_{\text{Maxwell}}$$
$$L_{\text{Maxwell}} = \frac{1}{n} \sum_{i=1}^n \left\| \widehat{H}_y - \nabla \times \left( \frac{1}{\varepsilon(\mathbf{r})\mu_0\omega^2} \nabla \times \right) \widehat{H}_y \right\|_2$$

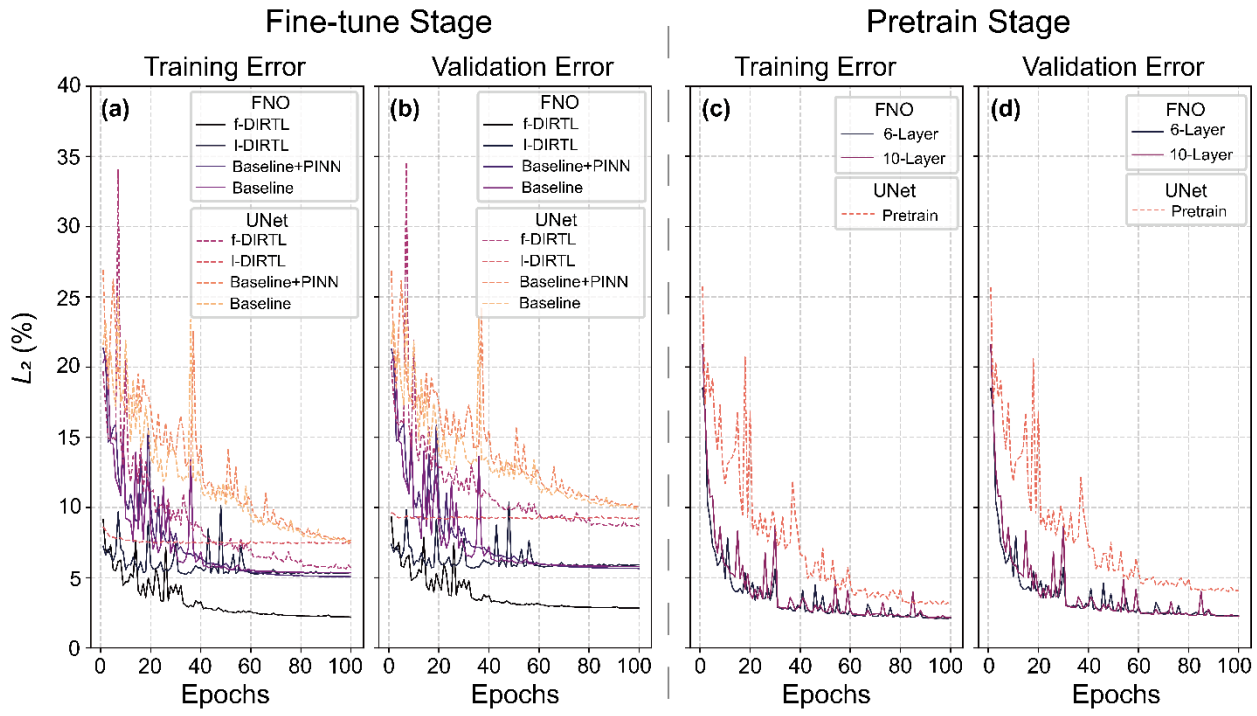
The term  $\alpha$  was dynamically tuned so that the ratio between  $L_{\text{MSE}}$  and  $\alpha \cdot L_{\text{Maxwell}}$  is constant. The ratio was chosen to be 0.05 for both FNO and UNet, which were all chosen via parameter sweep with learning rates identical to baseline training with only data loss [5]. The Maxwell loss itself was implemented by discretizing the frequency-domain Maxwell equations on a Yee grid [6].

### S4. Training Details on FNO and UNet

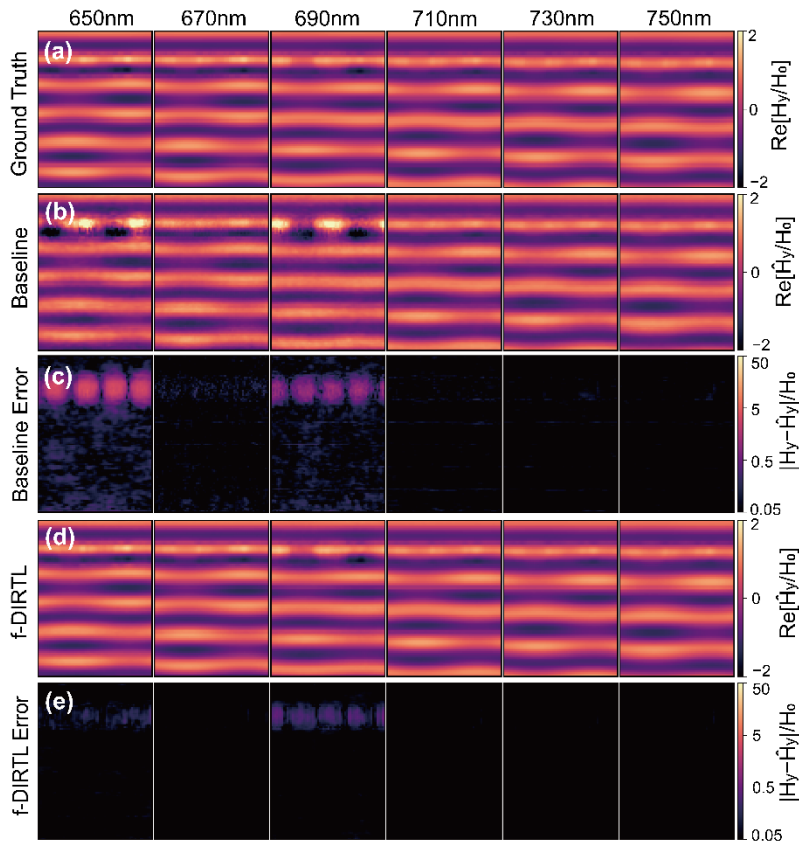
The hyperparameters for FNO and UNet used in this work are shown in Supplementary Table 1, while the learning rate scheduler parameters are shown in Supplementary Table 2. All training and test of models were done on NVIDIA® GeForce RTX™ 3080 GPU. The detailed architecture and l-DIRTL, f-DIRTL process for UNet is shown in Supplementary Fig 2 [7]. The training learning curve is shown in Supplementary Fig. 3. Supplementary Figure 4 shows overfitting examples, where neural network models falsely predict resonances where only background scattering occurs. Supplementary Figure 4 also demonstrates how f-DIRTL FNO suppresses such cases, increasing overall accuracy.



**Supplementary Figure 2 Architecture and DIRTl process for UNet.** (a) Detailed architecture for UNet used in EM inference for this work [7]. (b) I-DIRTL and (c) f-DIRTL process for UNet. In f-DIRTL, we transfer and freeze the downsampling encoding phase inside UNet architecture.



**Supplementary Figure 3 Learning curves of the models trained for comparison test.** Solid lines are those for FNO, while dotted lines are those for UNet. (a), (b) are training error and validation error for the fine-tune stages and the baseline training, while (c), (d) show training and validation for the pretrain stage.



**Supplementary Figure 4 Overfitting problem of baseline FNO** (a-e) Field distributions and prediction errors for a randomly selected test case at a 20 nm wavelength interval. (a) Ground-truth field distribution. (b) Baseline FNO prediction. (d) f-DIRTL FNO prediction. (c,e) Corresponding prediction-error maps for (c) the baseline FNO and (e) the f-DIRTL FNO. We see falsely predicted resonances in baseline FNO prediction, which doesn't happen for f-DIRTL FNO prediction.

**Supplementary Table 1** FNO and UNet hyperparameters

Model	Total Parameters	Hyperparameters		
FNO	10,496,162	Modes	16	Layers
		Width	32	Activation
		Depth	4	Initial Feature Maps
UNet	17,262,466	Convolution Kernel	3×3	Pooling
		Upsampling Kernel	2×2	Maxpool Kernel
		Scaling Factor	2	Activation
				ReLU

**Supplementary Table 2** Learning rate scheduler parameter for each training process

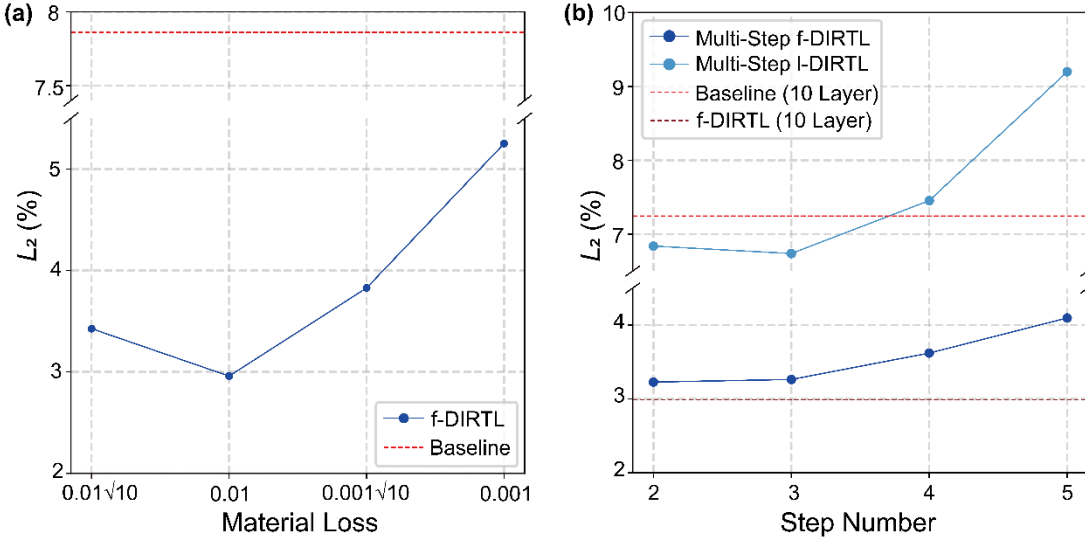
Model	Training Phase	Learning Rate Parameters		
		Initial Lr	Step Size	Gamma
FNO	Baseline	5e-4	10	0.5
	6-Layer Pretrain	1e-3	30	0.5
	10-Layer Pretrain	5e-4	30	0.5
	f-DIRTL	5e-3	10	0.7
UNet	l-DIRTL	5e-5	30	0.5
	Baseline	1e-4	20	0.5
	Pretrain	2e-4	20	0.5
	f-DIRTL	7e-5	20	0.6
	l-DIRTL	1e-6	15	0.3

## S5. Loss Tuning for Pretrain Stage

To see how much material loss is best, we demonstrated a simple sweep on different material absorption loss values. For this, we generated samples with  $k = 0.01\sqrt{10}, 0.01, 0.001\sqrt{10}, 0.001$ , with  $n = n_{mat} + ik$ , and pretrained on these to see which was best in the fine-tuned result. We pretrained and fine-tuned with respectively 1.5k structures sampled on 11 wavelength points, with pretrain stage datasets prepared on simulations with  $n = n_{mat} + ik$ . The f-DIRTL strategy was implemented with FNO model; 6-Layer FNO pretrained and transferred to 10-Layer fine-tuned model. The results in Supplementary Fig. 5(a) show that the loss we utilized;  $k = 0.01$ , was most effective, both in attenuating amplitudes to make a smooth learning field and preserving key mode characteristics.

## S6. Multi-Step DIRTL

To facilitate a smoother adaptation of the model toward learning resonant features, it is natural to adopt a multi-step learning process rather than the original two-step approach. Here, we implemented and tested multi-step DIRTL, where the material loss in the system is gradually decreased across steps. The optimizer and learning rate schedules were kept identical to those used in the two-step configuration. To ensure total data conservation, in an N-step process, the dataset for each step was set to  $(\text{total number of datasets})/N$  with total 6k different structures sampled on 11 wavelength points used.



**Supplementary Figure 5 Material loss sweep and multi-step DIRTl** (a) Results for f-DIRTL FNO with different material loss used in pretrain stage. (b) Test results for multi-step DIRTl FNO, compared to baseline FNO (red dotted) and 2-step f-DIRTL FNO (6-layer pretrain, 10-layer fine-tune, dark red dotted). Dark blue plot indicates multi-step f-DIRTL, while light blue plot indicates multi-step l-DIRTL

The l-DIRTL and f-DIRTL schemes were designed as follows, with the corresponding results shown in Supplementary Fig. 5(b). The  $k$  values used for each n-step configuration are summarized in the Supplementary Table 3. Since  $k = 0.01$  was found to be the most effective in earlier experiments, it served as the baseline for constructing the multi-step schedule. However, for the five-step process, because lower  $k$  values did not produce sufficient attenuation, we began with  $k = 0.01\sqrt{10}$  instead of adding smaller loss values at the end.

**Supplementary Table 3** Material loss schedule for each multi-step process' pretrain stage

Step Number	Material Loss	Step Number	Material Loss
2 Step	[0.01]	4 Step	[0.01, 0.001 $\sqrt{10}$ , 0.001]
3 Step	[0.01, 0.001 $\sqrt{10}$ ]	5 Step	[0.01 $\sqrt{10}$ , 0.01, 0.001 $\sqrt{10}$ , 0.001]

## l-DIRTL

As in the two-step Loose DIRTl, the model is fine-tuned at each step using the dataset corresponding to that step, without freezing any parameters.

## f-DIRTL

Analogous to the two-step process, after each step, additional Fourier layers are introduced and the model is fine-tuned using the dataset for that step. The training starts with four layers, and four more layers are added at each subsequent step. Consequently, an n-step process results in a model containing  $4 \times N$  Fourier layers.

For l-DIRTL, we observe a modest improvement in prediction accuracy when using a three-step process, followed by a degradation in performance as additional steps are introduced. This suggests that, in principle, a multi-step relaxation schedule can provide a smoother learning trajectory for l-DIRTL. However, as the number of steps increases, the reduced number of samples allocated to each step decreases, leading to reduced prediction accuracy for each step. As a result, for multi-step processes involving more than 3 steps, we see worse model capabilities. This trade-off is evident in Supplementary Fig. 5(b).

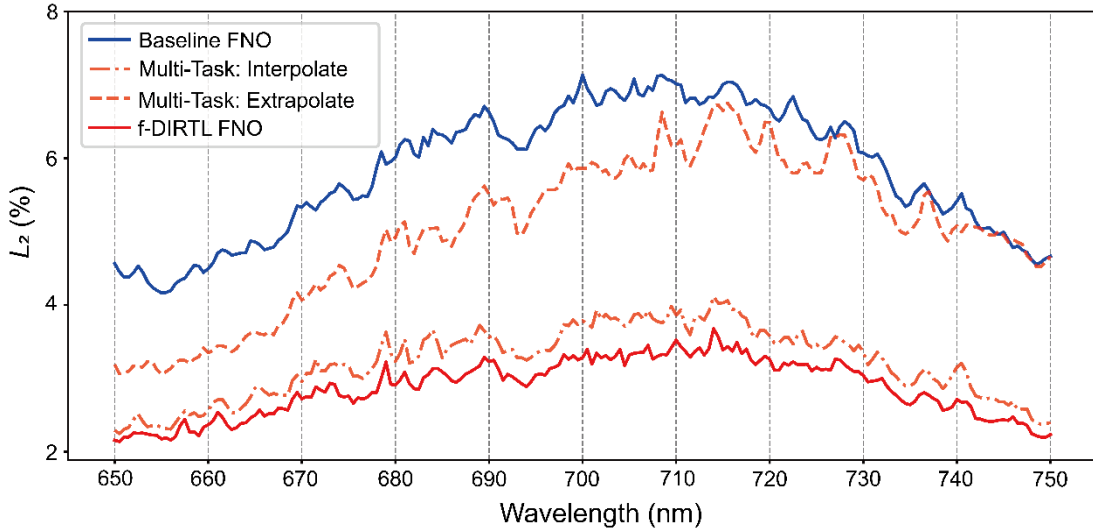
For f-DIRTL, Supplementary Fig. 5(b) shows that accuracy consistently worsens as the number of steps increases. In this case, the loss of accuracy caused by reducing the per-step dataset outweighs any benefit from smoother progressive learning. Consequently, a two-step DIRTL procedure emerges as the optimal configuration: it offers the most substantial performance gain for f-DIRTL while maintaining accuracy comparable to the best-performing configuration for l-DIRTL.

## S7. Multi-Task Performance of f-DIRTL FNO

To evaluate the generalizability of the proposed training strategy, we compare the predictive performance of the baseline FNO and f-DIRTL FNO on wavelengths during training. We generated 1,000 test samples uniformly sampled at 0.5 nm intervals. As shown in Supplementary Fig. 6, f-DIRTL FNO consistently achieves higher accuracy across the entire wavelength domain. To add to this, baseline FNO exhibits a pronounced increase in error near  $\sim 700$  nm, where most high-resonant cases occur. Meanwhile, f-DIRTL FNO suppresses this error curvature, demonstrating reliable performance even in resonance-dominated regimes where prediction is typically difficult.

The pretrained core also shows strong multi-tasking capabilities in both wavelength interpolation and extrapolation. In the interpolation setting, the model is first trained on a coarsely sampled wavelength grid (20 nm interval within 650–750 nm) and later fine-tuned on a denser grid (10 nm interval), using 4.5k structures for each

stage while following f-DIRTL FNO procedure. This entire process uses fewer training samples than the baseline model, which is trained directly on the dense wavelength grid with 9k structures. As shown in Supplementary Fig. 6, the interpolated f-DIRTL FNO achieves substantially lower prediction error across both trained and untrained wavelengths, demonstrating that the pretrained core encodes functionally meaningful wavelength-response relationships.



**Supplementary Figure 6 Multi-tasking evaluation of the f-DIRTL FNO.** This demonstrates comparison between the baseline FNO and f-DIRTL FNO on wavelength points not included in training. Gray dotted lines denote the 10nm training wavelengths; testing is performed at 0.5nm resolution across 1,000 structures. For interpolation multi-tasking case, the FNO model is pretrained 20nm interval wavelengths and fine-tuned on all 10nm training points. For extrapolation multi-tasking case, the f-DIRTL model is pretrained on the wavelengths 680nm ~ 720nm with 10nm intervals and fine-tuned on all 10nm training points.

More importantly, the pretrained core enables effective extrapolation, a significantly more challenging task for neural networks [8,9]. The compact model is first pretrained over the limited 680–720 nm region and then fine-tuned over the full 650–750 nm band, using 4.5k structures for each stage while following f-DIRTL FNO procedure. Even with fewer training samples than the baseline, the resulting model achieves higher accuracy in the previously unseen 650–680 nm region and comparable or improved accuracy in the 720–750 nm region, as shown in Supplementary Fig. 6. This demonstrates that the pretrained core forms wavelength representations that remain stable under spectral extension, enabling robust extrapolation.

Overall, these results indicate that the pretraining phase in f-DIRTL establishes a physically informed core representation that enables robust generalization across multiple wavelength inputs. This core representation can

be directly extended to related tasks, including wavelength interpolation and extrapolation, while preserving the data-efficiency of the approach. Although our demonstration focuses on multi-wavelength prediction, the same pretrained core has the potential to support broader multi-task learning scenarios—such as variations in incident angle, device geometry, or material refractive index—while still maintaining high training efficiency.

## References

- [1] Kim, Y., Jung, A. W., Kim, S., Octavian, K., Heo, D., Park, C., ... & Park, C. Y. (2024). Meent: Differentiable electromagnetic simulator for machine learning. *arXiv preprint arXiv:2406.12904*.
- [2] Lalanne, P., Yan, W., Vynck, K., Sauvan, C., & Hugonin, J. P. (2018). Light interaction with photonic and plasmonic resonances. *Laser & Photonics Reviews*, 12(5), 1700113.
- [3] Liu, V., & Fan, S. (2012). S4: A free electromagnetic solver for layered periodic structures. *Computer Physics Communications*, 183(10), 2233-2244.
- [4] Johnson, S. G., Ibanescu, M., Skorobogatiy, M. A., Weisberg, O., Joannopoulos, J. D., & Fink, Y. (2002). Perturbation theory for Maxwell's equations with shifting material boundaries. *Physical review E*, 65(6), 066611.
- [5] Mao, C., Lupoiu, R., Dai, T., Chen, M., & Fan, J. A. (2024). Towards general neural surrogate solvers with specialized neural accelerators. *arXiv preprint arXiv:2405.02351*.
- [6] Chen, M., Lupoiu, R., Mao, C., Huang, D. H., Jiang, J., Lalanne, P., & Fan, J. A. (2022). High-speed simulation and freeform optimization of nanophotonic devices with physics-augmented deep learning. *ACS Photonics*, 9(9), 3110-3123.
- [7] Krizhevsky, A., Sutskever, I., & Hinton, G. E. (2012). Imagenet classification with deep convolutional neural networks. *Advances in neural information processing systems*, 25.
- [8] Zhu, M., Zhang, H., Jiao, A., Karniadakis, G. E., & Lu, L. (2023). Reliable extrapolation of deep neural operators informed by physics or sparse observations. *Computer Methods in Applied Mechanics and Engineering*, 412, 116064.
- [9] Wang, Y., & King, R. D. (2024). Extrapolation is not the same as interpolation. *Machine Learning*, 113(10), 8205-8232.